

# Reconstruction algorithm study of 2D interpolating resistive readout structure<sup>\*</sup>

XIU Qing-Lei(修青磊)<sup>1,2,3;1)</sup> DONG Ming-Yi(董明义)<sup>1,2</sup> LIU Rong-Guang(刘荣光)<sup>1,2</sup>  
 ZHANG Jian(张建)<sup>1,2</sup> OUYANG Qun(欧阳群)<sup>1,2</sup> CHEN Yuan-Bo(陈元柏)<sup>1,2</sup>

<sup>1</sup> State Key Laboratory of Particle Detection and Electronics, Beijing 100049, China

<sup>2</sup> Institute of High Energy Physics, Chinese Academy of Sciences, Beijing 100049, China

<sup>3</sup> University of Chinese Academy of Sciences, Beijing 100049, China

**Abstract:** Systematic investigations including both simulation and prototype tests have been done about the interpolating resistive readout structure with GEM (Gaseous Electron Multiplier) detector. From the simulation, we have a good knowledge of the process of charge diffusion on the surface of the readout plane and develop several reconstruction methods to determine the hit position. The total signal duration time of a typical event with the readout structure was about several hundred nanoseconds, which implied an ideal count rate up to  $10^6$  Hz. A stable working prototype was designed and fabricated after the simulation. Using  $^{55}\text{Fe}$  5.9 keV X-ray, the image performance of the prototype was examined with flat field image and some special geometry shapes, meanwhile, an energy resolution of about 17% was obtained.

**Key words:** interpolating resistive readout structure, micro-pattern gaseous detector, Gaseous Electron Multiplier, two dimensional detectors, position reconstruction

**PACS:** 29.40.Cs, 29.40.Gx **DOI:** 10.1088/1674-1137/37/10/106002

## 1 Introduction

For Micro Pattern Gaseous Detectors, such as GEM (Gaseous Electron Multiplier) [1] and Micromegas [2], pixel pad is the most suitable readout structure. However, in order to obtain a good space resolution, one has to reduce the size of the pixel and employ a large amount of pixels to cover a required effective area, which leads to a dramatic increase of electronic channels. The virtual-pixel detector implemented with the two-dimensional interpolating resistive readout structure [3–5] which was developed by H. J. Besch can provide spatial resolution of about several hundred micro meters with an enormous reduction of electronic channels compared to pure pixel detectors. This readout structure that has high space resolution and low number of electronic channels is always a good option for many real applications.

With this concept, we do some numerical simulations and manufactured a GEM detector with two-dimensional interpolating resistive readout structure to have a good understanding of its performances.

## 2 Basic principles

### 2.1 Diffusion and collection of charge

We combined the resistive readout structure with a triple-GEM gas gain device in our detector development [6]. The electron cluster, generated by ionizing radiation and multiplied in an avalanche process in the triple-GEM region, will drift to the surface of 2D interpolating readout structure in the electric drift field, and then the charges will diffuse on the resistive plane and be collected by the readout nodes of the adjacent cells. Using the information of the collected charges, the hit position can be reconstructed with suitable algorithm.

With thick film process, the readout plane is assembled by cells consisting of a high resistivity square pad and low resistivity narrow strips, which can obtain fast time response and good position resolution. Each crossing point of the low resistive strips, the so-called readout node, is connected to a low input impedance readout channel. Combined with the nearest metal foil coated on the lower surface of GEM film, the readout structure

---

Received 6 December 2012, Revised 7 March 2013

\* Supported by Innovation Fund for Young Scholars of Institute of High Energy Physics

1) E-mail: xiuql@ihep.ac.cn

©2013 Chinese Physical Society and the Institute of High Energy Physics of the Chinese Academy of Sciences and the Institute of Modern Physics of the Chinese Academy of Sciences and IOP Publishing Ltd

can be treated as a distributed 2-dimensional resistive-capacitive network. The schematic of the resistive anode is illustrated in Fig. 1.

## 2.2 Basic reconstruction method

The position of the incident particle has an approximate linear relationship with charges ( $Q_i$ ) collected at the nodes of the adjacent cells. The simplest and most obvious linear reconstruction methods are so-called 4-, 6- and 3-node reconstruction algorithms. The node indications and the coordinate systems of the particular algorithms are also given in Fig. 1. The specified algorithms are listed below [7].

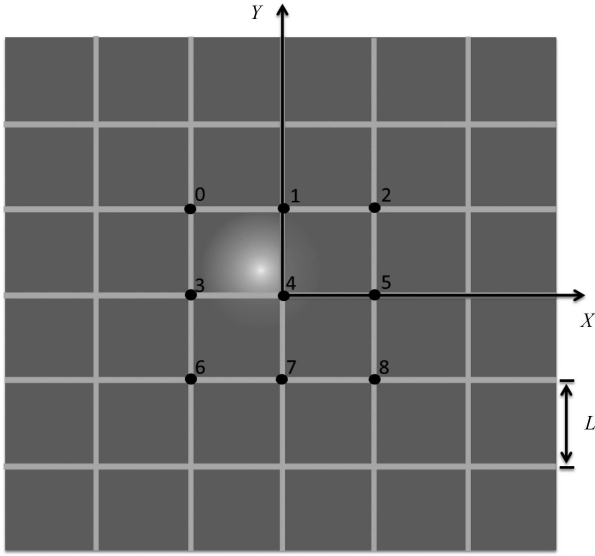


Fig. 1. Schematic illustration of resistive anodes. The edge length of a cell amounts to  $L=8$  mm. The surface resistance of the pad and strip is  $100 \text{ k}\Omega/\square$  and  $1 \text{ k}\Omega/\square$  respectively. Every crossing point of low resistive strip stands for a read-out node. To illustrate the basic reconstruction algorithms, 9 readout nodes are represented by a black point. The white point with halo stands for a typical event which is reconstructed with the following algorithms.

4-Anode Algorithm: The origin of the coordinate system is located at anode 3.

$$x_4 = L \frac{(Q_1+Q_4)-(Q_0+Q_3)}{Q_{\tau 4}}, \quad (1)$$

$$y_4 = L \frac{(Q_0+Q_1)-(Q_3+Q_4)}{Q_{\tau 4}}, \quad (2)$$

$$Q_{\tau 4} = Q_0+Q_1+Q_3+Q_4. \quad (3)$$

6-Anode Algorithm: Anode 4 is the origin.

$$x_6 = L \frac{(Q_2+Q_5)-(Q_0+Q_3)}{Q_{\tau 6x}}, \quad (4)$$

$$y_6 = L \frac{(Q_0+Q_1)-(Q_6+Q_7)}{Q_{\tau 6y}}, \quad (5)$$

$$Q_{\tau 6x} = Q_0+Q_1+Q_2+Q_3+Q_4+Q_5, \quad (6)$$

$$Q_{\tau 6y} = Q_0+Q_1+Q_3+Q_4+Q_6+Q_7. \quad (7)$$

3-Anode Algorithm: The origin is the same as 6-Anode Algorithm.

$$x_6 = L \frac{Q_5-Q_3}{Q_{\tau 3x}}, \quad (8)$$

$$y_6 = L \frac{Q_1-Q_7}{Q_{\tau 3y}}, \quad (9)$$

$$Q_{\tau 3x} = Q_3+Q_4+Q_5, \quad (10)$$

$$Q_{\tau 3y} = Q_1+Q_4+Q_7. \quad (11)$$

## 3 Simulation results

A numerical simulation was done to investigate the physical behaviors of 2D interpolating readout structure in our pre-research stage. With the simulation results, we can verify the reconstruction algorithms and know about the response time of this structure.

### 3.1 Mathematic model

In one dimension the resistive anode can be treated as a series connection of many identical small resistors which are parallel connected by many small capacitances formed by the metal foil of GEM and the surface of the resistive anode. The cross connection of the resistive-capacitive chain forms a two-dimensional network. The schematic of the model is illustrated in Fig. 2.

The equation describing the time evolution of the surface charge density when the charge is deposited on the resistive anode can be derived from Ohm's law and the conservation of electronic charge in this model.

Because the resistive anode is made of two different resistive materials, the resistance of the anode is spatially dependent. In fact, besides the metal foil of the GEM film, there are some metal wires behind the resistive anode board. However, the capacitance induced by the backside wire is very small and can be ignored to simplify the simulation. From the model in Fig. 2, denoting the constant capacitance by  $c$ , one can obtain the

surface charge density:

$$\vec{J} = \sigma \cdot \vec{E} = -\sigma \cdot \nabla V, \quad (12)$$

$$\rho(x, y, t) = c \cdot V(x, y, t). \quad (13)$$

Inserting (13) into (12), one can obtain:

$$\vec{J} = -\frac{\sigma}{c} \cdot \nabla \rho, \quad (14)$$

$$\nabla \cdot \vec{J} = -\frac{\partial \rho}{\partial t}. \quad (15)$$

Together with Ohm's law (14) and the conservation of electronic charge (15) the time derivative of the charge density can be obtained.

$$\frac{\partial \rho}{\partial t} - \frac{1}{c} [(\nabla \sigma) \cdot (\nabla \rho) + \sigma \nabla^2 \rho] = I(x, y, t). \quad (16)$$

$I(x, y, t)$ , which is assumed to be 2D Gaussian distribution in the spatial part and 1D Gaussian distribution in time since the transverse and longitudinal diffusion of the cluster in the gas [8], is used to simulate the current signal caused by incoming X-ray photons.

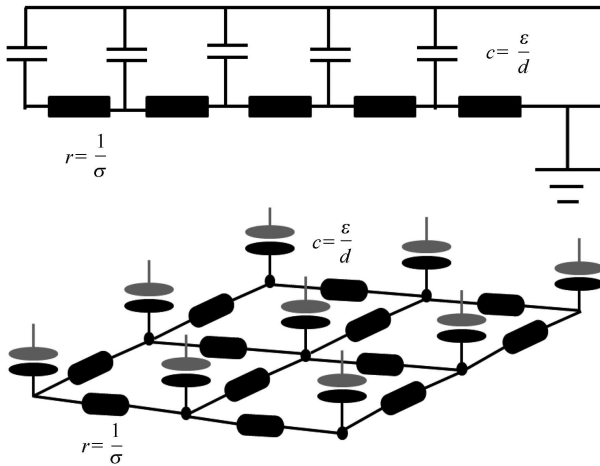


Fig. 2. Resistive-capacitive network model of the interpolating resistive readout structure. The continuous resistive plane is subdivided into small resistances which form a network. At every crossing node, a small capacitance contributed by GEM foil is connected. The simulation equation is derived from this model.

Because the input impedance of the electronic channel is much less than the resistance of the resistive strips, the readout nodes can be treated as ideal drains approximately, where the charge density is equal to zero at all times. This is regarded as the boundary condition of Eq. (16).

The analytic solution of this equation can't be obtained with this boundary condition. We transform the partial differential equation to the difference equation which can be solved with the numerical method.

To obtain the difference equation, the coordinates and time are subdivided into equal intervals  $\Delta x$ ,  $\Delta y$  and  $\Delta t$  [9]. The space-time coordinate of one grid point is  $(i\Delta x, j\Delta y, k\Delta t)$ . The schematic of the grid network is shown in Fig. 3. Every grid point is associated with particular properties such as  $\rho_{i,j,k}$  and  $\sigma_{i,j}$ . In order to take into account the cross diffusion of charges to neighbor cells and compare different reconstruction methods,  $3 \times 3$  cells are simulated. The time evolution of charge density can be transformed from Eq. (16):

$$\begin{aligned} \rho_{i,j,k+1} = & \rho_{i,j,k} \\ & + \frac{\Delta t}{2c\Delta x^2} \{[(\sigma_{i+1,j} + \sigma_{i,j})(\rho_{i+1,j,k} - \rho_{i,j,k}) \\ & - (\sigma_{i,j} + \sigma_{i-1,j})(\rho_{i,j,k} - \rho_{i-1,j,k}) \\ & + [(\sigma_{i,j+1} + \sigma_{i,j})(\rho_{i,j+1,k} - \rho_{i,j,k}) \\ & - (\sigma_{i,j} + \sigma_{i,j-1})(\rho_{i,j,k} - \rho_{i,j-1,k})]\} \\ & + I_{i,j,k} \Delta t, \end{aligned} \quad (17)$$

$$\frac{\sigma_{\max} \Delta t}{c \Delta x^2} \leq \frac{1}{4}. \quad (18)$$

This equation can be resolved in the numerical method with a recursive algorithm. To have a stable resolution, formula (18) must be satisfied when determining the interval  $\Delta x$  and  $\Delta t$  [10].

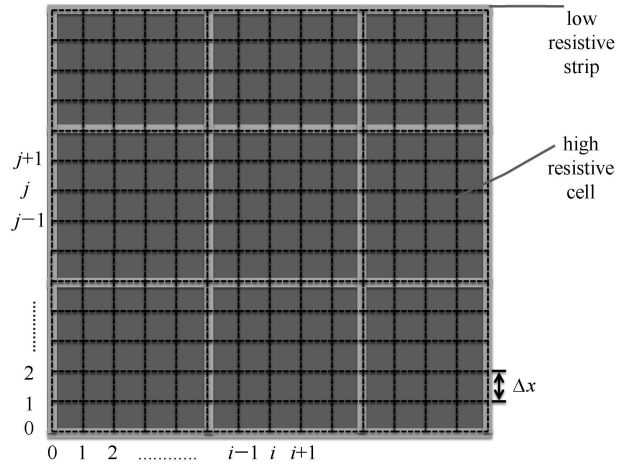


Fig. 3. Schematic of the grid network. The whole readout structure is subdivided into equal intervals by dashed lines. Every grid point is associated with particular properties such as  $\rho_{i,j,k}$  and  $\sigma_{i,j}$ .

After the building of the mathematic model, we develop a program to solve the model. The simulation results are shown below.

### 3.2 Charge diffusion

Most of the charges are collected by the four nodes at the corner of the cell. However, it's obvious that some charges will diffuse to neighboring cells through the low resistive strips, which will lead to some distortion of the reconstructed position. According to the theory analysis, increasing the ratio of the pad resistivity to the strip resistivity can reduce the cross diffusion. If the ratio of the high resistivity to the low resistivity is infinity, all charges will be collected in one cell. Nevertheless, the high resistivity is limited to less than  $1 \text{ M}\Omega/\square$  by count rate capability and the low resistivity is restricted to more than  $1 \text{ k}\Omega/\square$  by the resistive noise in real conditions. Fig. 4 shows the time evolution of charge density on the surface of the resistive anode with the resistivity of  $100 \text{ k}\Omega/\square$  for the pad and  $1 \text{ k}\Omega/\square$  for the strip respectively.

### 3.3 Time response

The charges diffuse on the surface of the resistive plane with a time constant which is related to the con-

ductivity  $\sigma$  and the capacitance  $c$ . The capacitance is fixed to be about  $5 \text{ nF}/\text{m}^2$  once the detector was manufactured with a distance of  $2 \text{ mm}$  between the GEM foil and the resistive plane. For the pad with resistivity of  $100 \text{ k}\Omega/\square$  and size of  $8 \text{ mm} \times 8 \text{ mm}$ , the charge collection time is about several hundred nanoseconds. Considering the drift time of electrons in the gas, the total time of one event in the detector is about several hundred nanoseconds [11]. Equipped with suitable electronics, the count rate of the system can approach up to  $10^6 \text{ Hz}$ .

The current signals of events at different distances from the collecting node are shown in Fig. 5; one can see that the duration time of the signal is about several hundred nanoseconds.

### 3.4 Reconstruction

In the simulation, we can adjust the input position of the incoming current signal in one pad to form a simulated flat pattern (Fig. 6(a)). With the reconstruction method mentioned before, we can obtain the reconstructed pattern which can be compared with the flat pattern.

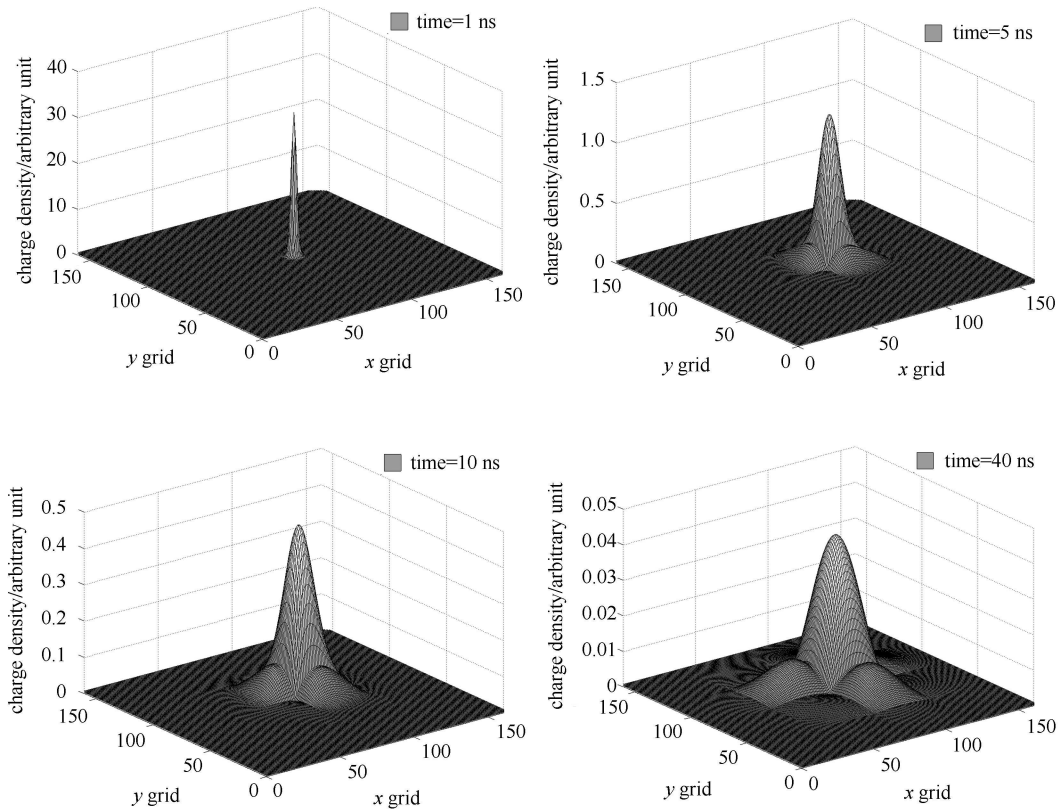


Fig. 4. Time evolution of the charge density. At the beginning, charges are concentrated in a very small region with a high charge density. With the diffusion and collection of the charges, the distribution of the charges becomes wider and more tenuous. From the last distribution graph, the low resistive strips and the readout nodes can be recognized clearly.

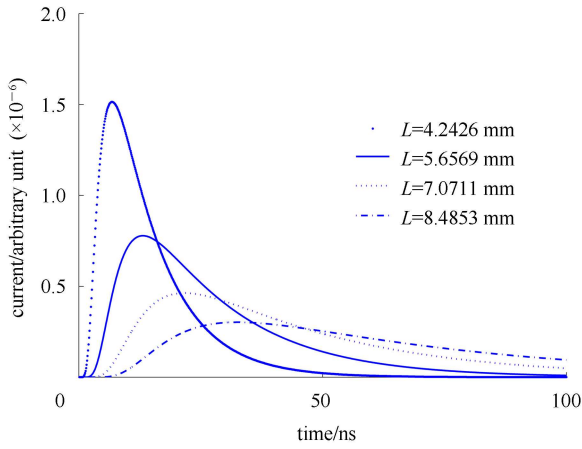


Fig. 5. Current signals of events at different distances from the readout node. The length of one cell is 8 mm. According to this result, the majority of charges are collected in several hundred nanoseconds for high resistivity  $100 \text{ k}\Omega/\square$ .

In Fig. 6(b)–6(d), the reconstructed positions in one pad of the 4-, 3- and 6-node algorithm are shown. The

four-anode algorithm shows perfect reconstructions at the center of the cell, whereas the hits close to the strip are distorted. In contrast to the four-anode algorithm, both the 3- and 6-node algorithm have large distortions in the cell center, however, they are more suitable for the hits close to borders of the cell. The similarity of reconstruction behavior of the 3- and the 6-node algorithm comes from the use of comparable symmetry planes and readout nodes.

In order to reconstruct the hit positions with fewer distortions, a new algorithm, the so-called weighted average algorithm, is introduced (Fig. 6(e)). The following equations define this algorithm.

$$x_m = a_x x_4 + (1 - a_x)[b_x x_3 + (1 - b_x)x_6], \quad (19)$$

$$y_m = a_y y_4 + (1 - a_y)[b_y y_3 + (1 - b_y)y_6]. \quad (20)$$

Since the position reconstructed from the 3- and 6-node algorithm is very similar, we set  $b_x = b_y = 0.5$ , which means that the weight of the 3- and the 6-node algorithm is equal. However, it's obvious that the weight  $a_x$  and  $a_y$  are position dependent. The weight of 4-node algo-

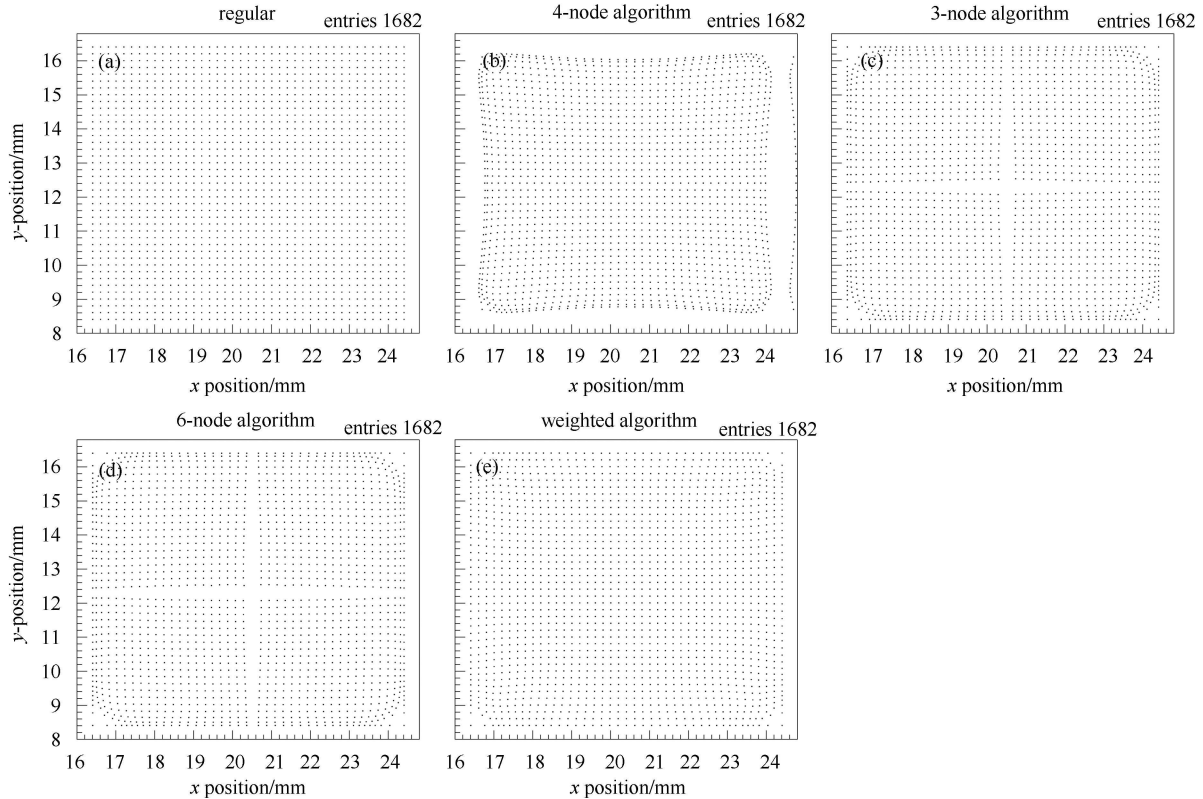


Fig. 6. Comparison between real position and reconstructed position of the simulated flat pattern in one pad. The real position of the flat pattern is shown in (a). (b,c,d,e) is reconstructed with 4-, 6- and 3- and weighted average algorithm. The distortion is larger at the border for 4-node algorithm (b) and larger at the central part of the pad for 3-, 6-node algorithms (c, d). With the weighted average algorithm (e), the hit position is well reconstructed.

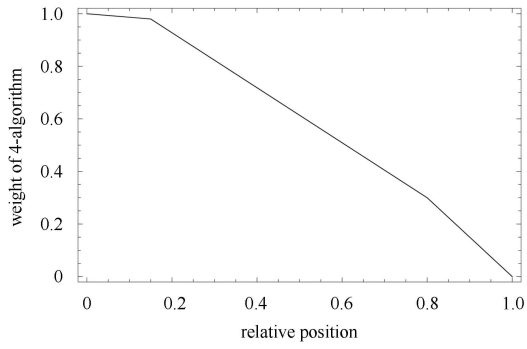


Fig. 7. The weight of 4-node algorithm in the weighted average algorithm. The  $x$  coordinate is the relative position of the event. 0 means the center of the cell and 1 means the border. The  $y$  coordinate stands for factors  $a_x$  and  $a_y$ , the weight of 4-node algorithm, in equations (19) and (20). This function can be tuned with measured results.

thm should be large at the center of the cell and becomes smaller and smaller when approaching the borders. We

find a piecewise continuous linear function to describe the position dependence of  $a_x, a_y$ . The graph of the function is shown in Fig. 7. In real conditions, the weights  $a_x$  and  $a_y$  should be tuned with a standard measurement first.

A quality comparison of the  $x$  distribution between the real position and the reconstructed position of the simulated flat pattern is shown in Fig. 8. The reconstruction effect of the weighted average algorithm is much better than other algorithms. The  $\chi^2$  of the weighted average algorithm is too small because the electronics noise and other random factors are not considered in the simulation. In real conditions, it is impossible for the reconstruction to be so perfect.

### 4 Test results

With the simulation results, we design and fabricate a triple-GEM prototype [6]. The resistivity of the pad is set to be  $100 \text{ k}\Omega/\square$  and the strip to be  $1 \text{ k}\Omega/\square$ , which has a fast response time and keeps the charge losses small.

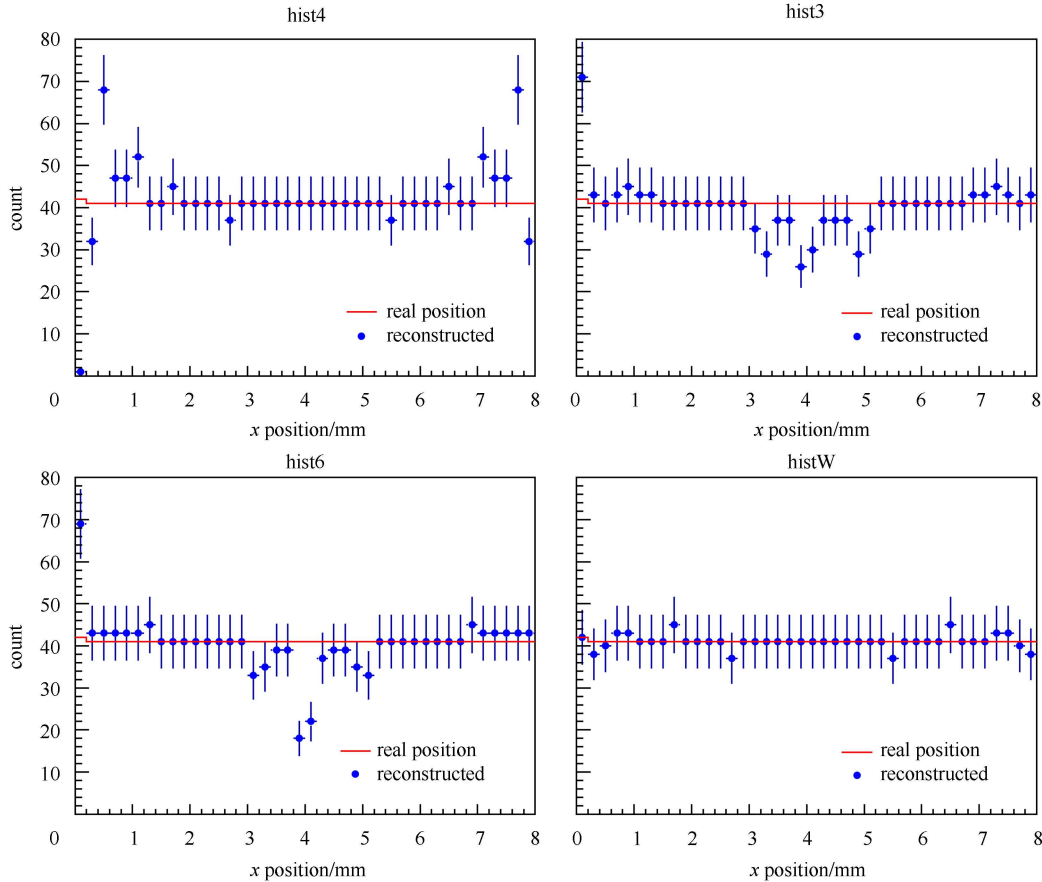


Fig. 8. The comparison of the  $x$  distribution between the real position and the reconstructed position of the simulated flat pattern with 4-, 3-, 6-node and weighted average algorithm. The  $\chi^2$  value of the four comparisons are 90.51, 40.76, 46.48 and 2.44 with the ndf of 39 respectively. The  $\chi^2$  of weighted average algorithm is too small, because the simulation is done in the ideal conditions.

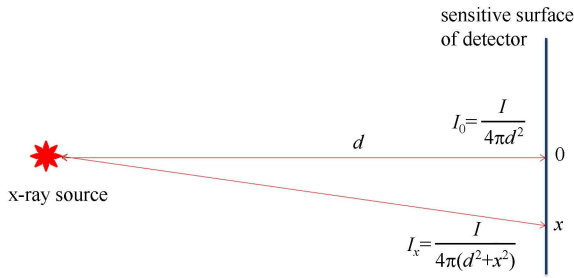


Fig. 9. The setup of the flat field test. In the area of one pad, the relative difference of intensity at the sensitive surface of the detector is less than 2.55%, which means the X-ray field can be assumed to be a very good flat field

#### 4.1 Image performance

The image performance of the prototype is studied using  $3 \times 3$  cells with  $^{55}\text{Fe}$  5.9 keV X-ray source. The setup of the test is shown in Fig. 9. The relative difference of intensity at different points is  $\frac{I_0 - I_x}{I_0} = \frac{x^2}{x^2 + d^2}$  for a dot-like X-ray source. For a pad with scale  $8 \text{ mm} \times 8 \text{ mm}$  and the distance  $d = 35 \text{ mm}$ , the maximum difference is 2.55%. The difference will be much smaller for a plane X-ray source. Thus the X-ray field can be assumed to be a very good flat field in the area of one pad.

##### 4.1.1 Calibration of the reconstruction algorithm

The resistive readout GEM detector should first be calibrated after assembly. A flat field image shown in Fig. 10 is obtained with X-ray to tune the parameter set of the weighted average algorithm. For the events in the central pad of the flat field image, the position distribution in one direction is assumed to be uniform. When the reconstruction parameter set is modified, the reconstructed position distribution will be different. Thus we can compare the reconstructed position distribution with the uniform distribution and obtain the  $\chi^2$  value. After a wide range scanning of the reconstruction parameter sets, the set with least  $\chi^2$  value is selected to be the optimum parameter set. Because the reconstruction of  $x$  and  $y$  position are independent, the calibration of  $x$  and  $y$  dimension should also be done separately. Fig. 11 shows the comparison between the uniform distribution and the reconstructed distribution with 4 different parameter sets.

After the detector is calibrated, the parameter set of the weighted average algorithm can be stably used unless some parameters of the detector are changed. The calibrated flat field image of  $3 \times 3$  pads, which is divided by the dashed line, is shown in Fig. 10.

##### 4.1.2 Image of a small hole

Collimating the X-ray source with a small hole, we

can get an image of the small hole. The image reconstructed with the weighted average algorithm is shown in Fig. 12. All the parameters are obtained from the flat field tuning.

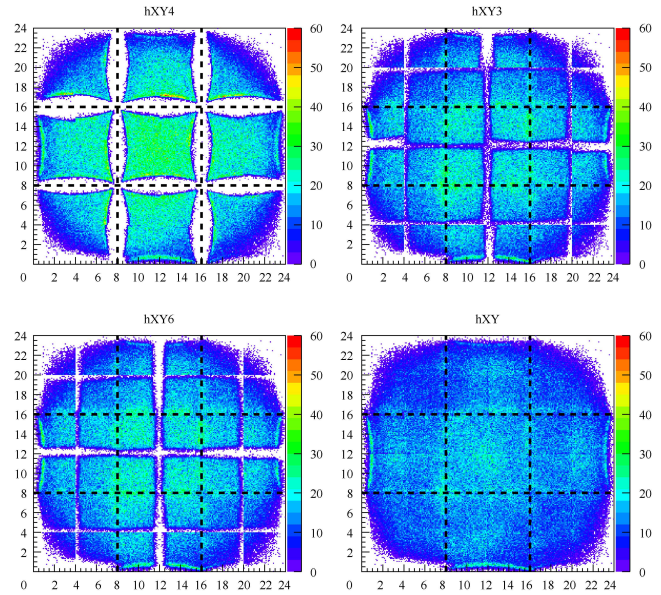


Fig. 10. The flat field images of  $3 \times 3$  pads are reconstructed with 4-, 3-, 6-node and weighted average algorithm respectively. The dashed line represents the border of one pad. The absence of events at the four corners is caused by the trigger setup. The events in the central pad are used to tune the reconstruction parameters.

#### 4.2 Comparison between the simulation and the test results

In Fig. 6 we have investigated the reconstruction effect of the 4-, 3-, 6-node and weighted average algorithm with a simulated flat field pattern. After the X-ray flat field test in Fig. 11, we can make a comparison of reconstructed position between the simulated flat field pattern and the X-ray flat field image to verify the correction of the simulation model in Eq. (17). The normalized comparison of reconstructed  $y$  distribution is shown in Fig. 13, which illustrates that the simulation is consistent with the test results on the whole.

The simulation doesn't take into account the noise of the electronics, the inhomogeneity of the resistive film and the fabrication error of the resistivity and so on, thus it's inevitable that there exist some differences between the simulation and the test results. The consistency between the simulation and real detector can be improved when considering these factors. The distributions in  $x$  direction show similar behaviors as the  $y$  direction.

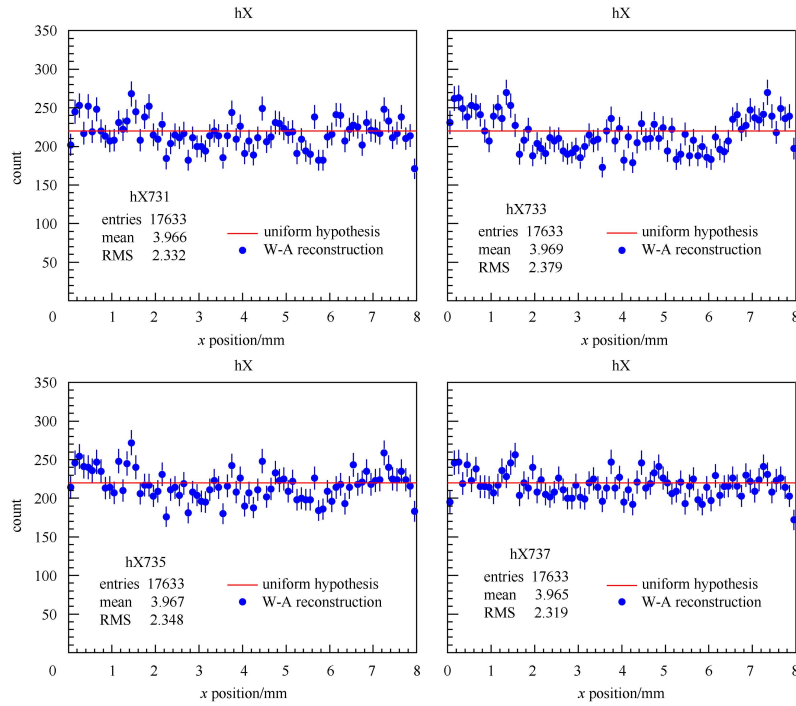


Fig. 11. The comparison between the uniform distribution and the reconstructed distribution in the central pad of Fig. 10 with 4 different parameter sets. The  $\chi^2$  value of the four comparisons are: 139.62, 205.66, 142.77 and 93.32 with the ndf of 79. A good reconstruction will give a lower  $\chi^2$  value, thus the  $\chi^2$  can be used as the evaluation criteria to optimize the reconstruction parameter.

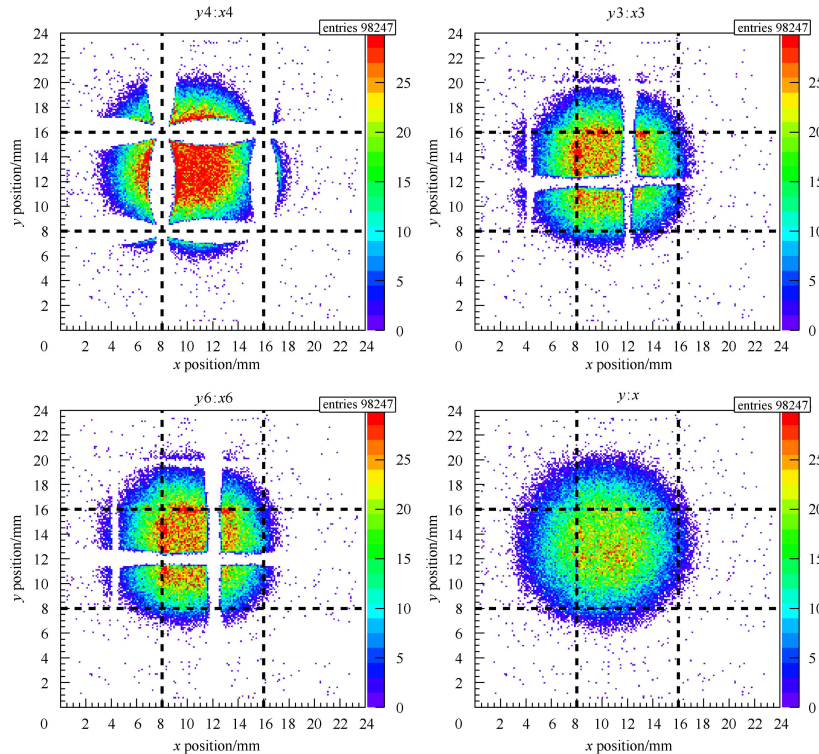


Fig. 12. The image of a small hole with diameter of  $4.67 \pm 0.01$  mm. The thickness of the hole is  $13.88 \pm 0.02$  mm and the distance from the hole to the sensitive surface of the detector is  $13 \pm 1$  mm. A homogeneous plane X-ray source sticks to the surface of the hole. The projection diameter of the hole on the sensitive surface is about 13 mm through a simple geometry calculation, which agrees with the image very well.

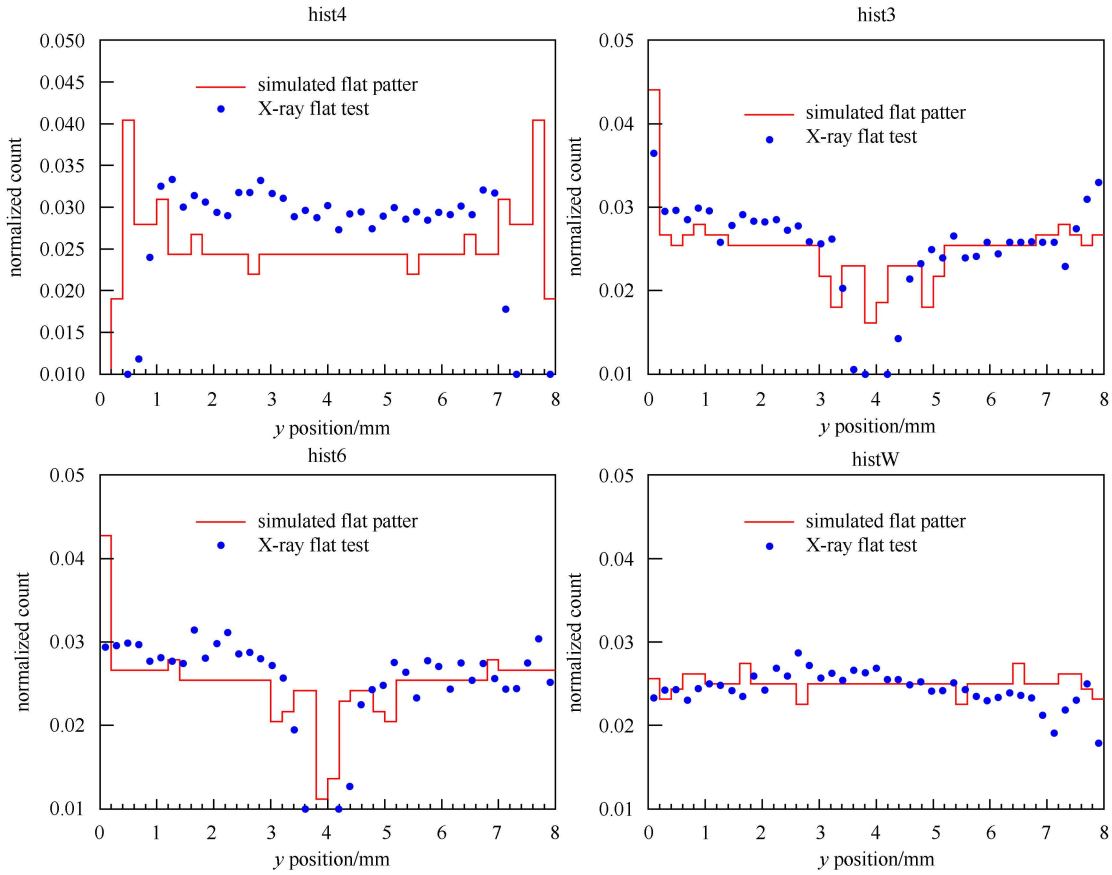


Fig. 13. The normalized comparisons of reconstructed  $y$  distributions between the simulated flat pattern in Fig. 6 and the X-ray flat field test in the central pad of Fig. 10 with 4-, 3-, 6-node and weighted average algorithm. The distribution is approximately uniform for the weighed average algorithm, while entries in the central part of the pad are obviously low for 3 and 6-node algorithm. There exist some differences between the simulation and the X-ray test because the simulation is done in ideal conditions.

### 4.3 Spatial resolution

The spatial resolution at the central part of one resistive pad has been tested in reference [6], which gives the best spatial resolution  $r$  of 219  $\mu\text{m}$  (FWHM). At the edge and the corner of the pad, the distortion  $d$  could be considered as a systematic error of the reconstructed position, thus the total spatial resolution can be estimated as  $\sqrt{r^2+d^2}$  according to the error theory. With the simulation results, the spatial resolution vs. the real position in one pad is shown in Fig. 14.

In fact, the spatial resolution is related to the charge collection time and the size of the pad.

A full collection of charges leads to the best spatial resolution, however, the time of charge collection will be too long. According to the simulation results, a charge integration time of several hundred nanoseconds is enough for a good spatial resolution with the resistivity of  $100 \text{ k}\Omega/\square$ .

Another factor that affects the spatial resolution is the size of the pad. Larger pad scale will lead to longer

charge collection time and worse spatial resolution, thus the pad scale should be adjusted according to the requirements of spatial resolution. A conservative estimate shows that the size of the pad could be up to  $20 \text{ mm} \times 20 \text{ mm}$  with a global spatial resolution less than 1 mm.

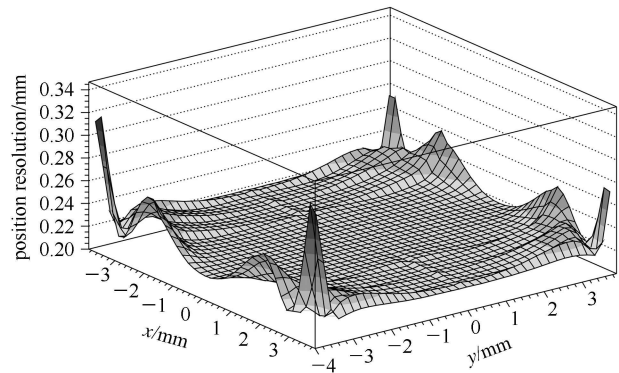


Fig. 14. Spatial resolution at different points in one pad. The resolution at the corner is about 50% worse than the central part.

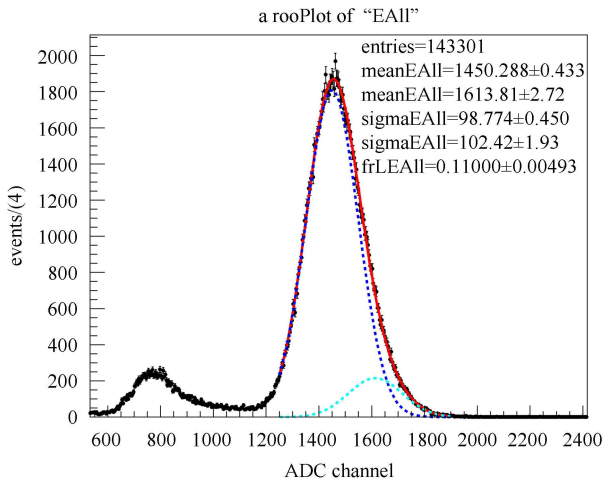


Fig. 15. Energy spectrum of  $^{55}\text{Fe}$  5.9 keV X-ray. The energy resolution of the prototype is about 17.4%@5.9 keV taking account of the influence of 6.49 keV X-ray which accounts for about 10.5% of the total photon flux.

#### 4.4 Energy resolution

Since the charges of one event can be fully collected, we can obtain the energy spectrum deposited in the detector Fig. 15.

The energy spectrum isn't an ideal Gaussian shape, because the X-ray photons emitted from  $^{55}\text{Fe}$  consist of 5.9 keV and 6.49 keV level. The two levels are too close to separate in our detector. We use a double Gaussian function to fit the data. The energy resolution is about 17.4% at 5.9 keV, and the ratio of 6.49 keV peak channel to 5.9 keV peak channel is  $1.113 \pm 0.002$ , which is consistent with the theoretical value.

## 5 Conclusion

Systematic investigations about the 2-Dimensional

interpolating resistive readout structure have been done in the development of a GEM prototype.

A mathematic model was built to simulate the charge diffusion process at the resistive surface, and to determine the key parameters such as resistivity, and pad scale of the resistive readout structure. For the pad with resistivity of  $100 \text{ k}\Omega/\square$  and size of  $8 \text{ mm} \times 8 \text{ mm}$ , the total signal duration time of a typical event is about several hundred nanoseconds. These simulation results imply that the readout structure has potential to approach a count rate of  $10^6 \text{ Hz}$ .

Because the simple linear reconstruction algorithms that just use the charges collected by 4 nodes of a cell have a defect for the hits close to the border of the cell, a weighted average algorithm combining 3 basic linear algorithms is introduced. In this algorithm, the position is reconstructed with the 3, 4, 6-nodes method respectively at the first step and then an average position is obtained with different weights for 3 basic linear algorithms. With correct calibrations and optimizations, the distortion caused by charge loss close to the cell border can be significantly suppressed.

The GEM prototype was tested with  $^{55}\text{Fe}$  X-rays. Using the weighted average reconstruction algorithm, the prototype has a very good image performance. The energy resolution of the prototype is about 17% when taking into account the two energy levels of  $^{55}\text{Fe}$  X-rays.

From the simulations and prototype tests, we can see that the interpolating resistive readout structure has good time resolution and image performance with low number of electronic channels. With these advantages, wide applications of this interpolating readout structure for micro-pattern gaseous detector can be expected.

*We are especially indebted to Prof. Xie Yi-gang, Dr. Fan-RuiRui and Dr. Lv-Xinyu for their useful suggestions and discussions.*

## References

- Sauli F. Nucl. Instrum. Methods A, 1997, **386**(2-3): 531
- Giomataris Y, Rebourgeard Ph, Robert J P et al. Nucl. Instrum. Methods A, 1996, **376**(1): 29
- Besch H J, Junk M, Meißner W et al. Nucl. Instrum. Methods A, 1997, **392**(1-3): 244
- Sarvestani A, Besch H J, Junk M et al. Nucl. Instrum. Methods A, 1998, **419**(2-3): 444
- Orthen A, Wagner H, Besch H J et al. Nucl. Instrum. Methods A, 2002, **478**(1-2): 200
- DONG Ming-Yi, XIU Qing-Lei, LIU Rong-Guang et al. CPC(HEP & NP), 2013, **32**(2): 026002
- Wagner H, Orthen A, Besch H J et al. Nucl. Instrum. Methods A, 2004, **523**(1-2): 287
- Dixit M S, Rankin A. Nucl. Instrum. Methods A, 2006, **566**: 281-285
- Wagner H, Besch H J, Menk R H et al. Nucl. Instrum. Methods A, 2002, **482**(1-2): 334
- LU Jun-An, SHANG Tao et al. The Resolution of Partial Differential Equation with Matlab. Wuhan: Wuhan University Press, 2002.148-149 (in Chinese)
- Bachmann S, Bressan A et al. Nucl. Instrum. Methods A, 1999, **438**(1): 376